INTERNATIONAL JOURNAL OF PHARMACOGNOSY AND CHEMISTRY
Content available at www.saap.org.in Online ISSN: 2582-7723

Open Access Research Article

SYNTHESIS, SPECTROSCOPIC AND STRUCTURAL CHARACTERISATION, DFT STUDY AND IN VITRO BIOLOGICAL EVALUATION OF A BENZIMIDAZOLE–AZO FUNCTIONALISED 1,3-BENZOXAZEPINE-1,5-DIONE

RAWAA NAEAMAH ABDULLAH

Ministry of Education, General Directorate of Al-Qadisiyah Education, Diwaniyah, Iraq

DOI: https://doi.org/10.46796/ijpc.v7i2.948

ARTICLE HISTORY

Received on: 27-05-2026
Revised on: 11-06-2026
Accepted on: 21-08-2026

Keywords: *1,3-Benzoxazepine; Benzimidazole; Azo dye; [2+5] cycloaddition; Powder X-ray diffraction; Density functional theory; MTT assay; HepG2*

***CORRESPONDING AUTHOR**
Rawaa Naeamah Abdullah

ABSTRACT

A novel seven-membered oxygen/nitrogen heterocycle containing benzimidazole, azo, and phenolic pharmacophores was synthesized in four steps and evaluated in vitro. Condensation of o-phenylenediamine with salicylaldehyde afforded 2-(1H-benzimidazol-2-yl)phenol, followed by azo coupling with diazotized 4-aminoacetophenone, condensation with benzocaine, and [2+5] cycloaddition of the resulting ketimine with phthalic anhydride. The target compound, ethyl 4-[3-(4-{[3-(1H-benzimidazol-2-yl)-4-hydroxyphenyl]diazenyl}phenyl)-3-methyl-1,5-dioxo-1,5-dihydro-4H-benzo[e][1,3]oxazepin-4-yl]benzoate (13), was obtained as a red solid in 79% yield (m.p. 280–282 °C). FT-IR and ^{13}C NMR data confirmed ring formation, with lactone and lactam carbonyl bands at 1712.67 and 1689.53 cm^{-1} and three carbonyl resonances at 167.03, 166.36, and 165.78 ppm. Powder X-ray diffraction indicated a predominantly amorphous structure with residual crystalline sodium chloride. B3LYP/6-31G(d)//GFN2-xTB calculations showed 228 real vibrational modes, a HOMO–LUMO gap of 3.592 eV, chemical hardness of 1.796 eV, and electrophilicity of 3.867 eV. The azo bridge contributed substantially to LUMO localization and electronic conjugation, while an intramolecular O–H···N hydrogen bond (1.690 Å) stabilized the structure. In vitro evaluation against HepG2 cells showed 53.4% viability at 400 µg mL^{-1}, whereas WRL-68 cells retained 80.8% viability, indicating preferential cytotoxicity toward hepatocellular carcinoma cells.

This article is licensed under a Creative Commons Attribution-Non-commercial 4.0 International License. Copyright © 2026 Author(s) retains the copyright of this article.

1. INTRODUCTION

Seven-membered rings carrying both oxygen and nitrogen occupy an unusual position in heterocyclic chemistry. They are conformationally flexible, which makes them harder to characterise than their five- and six-membered relatives, and yet the 1,3-oxazepine framework appears in compounds with antibacterial, antifungal, anti-inflammatory, antitumour and antidepressant activity, and a recent review of multicomponent approaches makes clear that interest in the ring is still growing [1]. The related six-membered oxazine scaffold has attracted comparable attention as a pharmacophore in drug discovery [2].

The established route to these rings is a two-step sequence in which an aromatic carbonyl compound is first condensed with a primary aromatic amine to give a Schiff base, and the imine is then treated with a cyclic anhydride in a dry aprotic solvent under reflux [3–6]. The transformation is written as a [2+5] cycloaddition: the imine nitrogen and the anhydride combine so that the five-membered anhydride ring opens and its two carbonyl carbons become, respectively, the lactam and the lactone carbon of the new seven-membered ring. Because nothing is expelled, the product is the simple 1:1 adduct of the two partners, which makes the mass balance a useful check on the assignment. Maleic anhydride delivers 1,3-oxazepine-4,7-diones that retain a ring C=C bond, whereas phthalic anhydride delivers the benzo-fused analogues, the 1,5-dihydrobenzo[e][1,3]oxazepine-1,5-diones [3, 4, 6].

Oxazepines obtained by this route have been reported with antibacterial and antifungal activity [5, 7–9], with antioxidant activity measured by DPPH and hydroxyl-radical scavenging [10, 11], and, in one study of sulfonamide-derived oxazepines, with a combination of antimicrobial and antioxidant activity and low cytotoxicity supported by DFT and docking [12]. Docking of bis-benzoxazepines against the progesterone receptor has also suggested anticancer potential [6].

The benzimidazole nucleus is one of the most heavily exploited pharmacophores in medicinal chemistry, and reviews of the scaffold list anticancer, antibacterial, antifungal, antiviral, antihypertensive and antiulcer applications [13]. Benzimidazole-derived Schiff bases in particular combine antimicrobial and antiproliferative activity [14–16], and several benzimidazole hybrids have been screened against cell-line panels that include the HepG2 hepatocellular carcinoma line [17–20]. The most potent examples reach the low-micromolar or sub-micromolar range: IC_{50} values of 3.22 μM have been reported for a trisubstituted benzimidazole [21] and 6.56 μM for a benzimidazole–triazole hybrid [20], while a 2-phenylbenzimidazole series reaches sub-micromolar potency [22]. Others are considerably weaker, at 25.1 μM [18] or 7–30 μg mL^{-1} [19]. The azo linkage is a second useful element: it is planar, strongly conjugating, and appears in dyes whose biological profiles have been examined alongside their optical properties; benzimidazole-(aryldiazenyl) hybrids have been evaluated against both Staphylococcus aureus and Escherichia coli and against HepG2 [17]. A phenolic hydroxyl completes the set, contributing hydrogen bonding and a site for hydrogen-atom transfer.

The compound reported here brings all three groups onto a single benzoxazepine framework. We describe its four-step synthesis, its characterisation by FT-IR and by ^{1}H and ^{13}C NMR spectroscopy, its powder X-ray diffraction pattern, a computational study of its electronic structure, and its cytotoxicity against the HepG2 hepatocellular carcinoma line measured in parallel with the normal WRL-68 hepatocyte line. Benzimidazole-tethered oxazepines that carry no azo bridge have already been characterised crystallographically and at a comparable DFT level, and their frontier-orbital gaps provide a point of comparison for the electronic descriptors reported here [23].

2. MATERIALS AND METHODS

2.1. Chemicals and instrumentation

o-Phenylenediamine, salicylaldehyde, 4-aminoacetophenone, benzocaine (ethyl 4-aminobenzoate), phthalic anhydride, sodium nitrite, sodium hydroxide, sodium carbonate, urea, hydrochloric acid (37%, 11.7 M), anhydrous calcium chloride, spectroscopic-grade potassium bromide, 1,4-dioxane, absolute ethanol, glacial acetic acid, chloroform, methanol, ethyl acetate, n-hexane and dimethyl sulfoxide were of analytical reagent grade and were used as received without further purification. The 1,4-dioxane used in the ring-forming step was dried over sodium wire and distilled immediately before use, and distilled water was used throughout.

Reaction progress and product purity were monitored by thin-layer chromatography on pre-coated silica-gel 60 F_{254} aluminium plates of 0.2 mm layer thickness, developed with ethyl acetate–n-hexane (1:1, v/v) for compound 1 and with chloroform–methanol (9:1, v/v) for compounds 2, 9 and 13; spots were visualised under a UV lamp at 254 nm. Each reaction was taken to be complete when the spot of the starting material being monitored was no longer detectable, and each purified product gave a single spot.

Melting points were determined in open capillary tubes at a heating rate of 1 °C min^{-1} on a Gallenkamp melting-point apparatus (Sanyo Gallenkamp, Loughborough, UK) and are uncorrected. Infrared spectra were recorded as potassium bromide discs, prepared from about 1 mg of sample dispersed in 100 mg of spectroscopic-grade KBr and pressed under 10 t, over the 4000–400 cm^{-1} range on a Shimadzu IRAffinity-1 FT-IR spectrophotometer (Shimadzu Corporation, Kyoto, Japan) at a nominal resolution of 4 cm^{-1}, thirty-two scans being averaged against a blank KBr background.

^{1}H and ^{13}C NMR spectra were recorded on a Bruker Avance III spectrometer operating at 400.13 MHz for ^{1}H and 100.61 MHz for ^{13}C, at 298 K, with DMSO-d_6 as solvent; ^{1}H chemical shifts are referenced to internal tetramethylsilane at δ 0.00 ppm and ^{13}C chemical shifts to the DMSO-d_6 septet at δ 39.5 ppm. Powder X-ray diffraction data were collected on a Shimadzu XRD-6000 diffractometer (Shimadzu Corporation, Kyoto, Japan) with Cu $K\alpha_1$ radiation (λ = 1.54060 Å) over 5–80° 2θ in steps of 0.04° with a counting time of 1.0 s per step, a fixed 1.0° divergence slit and a 0.1 mm receiving slit, at 25 °C. Elemental analysis and high-resolution mass spectrometry have not been carried out on the final compound; only the calculated values are quoted in Section 2.5, and Section 3.11 states what the measurements would add.

2.2. 2-(1H-Benzimidazol-2-yl)phenol (1)

o-Phenylenediamine (2.163 g, 20.0 mmol) and salicylaldehyde (2.442 g, 2.13 mL, 20.0 mmol, 1.00 equiv) were dissolved in absolute ethanol (40 mL) in a 100 mL round-bottomed flask fitted with a reflux condenser open to the air, glacial acetic acid (5 drops, ca. 0.25 mL) was added as catalyst, and the equimolar mixture was heated under reflux at 78 °C with magnetic stirring for 6 h. The condensation proceeds through the mono-Schiff base, which cyclises to the 2-aryl-2,3-dihydro-1H-benzimidazole; that dihydro intermediate is the two-electron reduced form of the product and aromatises to the benzimidazole by aerial oxidation, which is why the reaction is run open to the atmosphere [13]. Progress was followed by TLC (ethyl acetate–n-hexane, 1:1, v/v) until the o-phenylenediamine spot had disappeared. The solution was concentrated to about half its volume under reduced pressure, allowed to cool, and poured onto crushed ice (100 mL) with stirring. The precipitate was collected by suction

filtration, washed with cold ethanol–water (1:4, v/v, 3 × 15 mL) and then with cold distilled water until the washings were neutral, dried in air and recrystallised from absolute ethanol to give 1, $C_{13}H_{10}N_2O$, M = 210.23 g mol^{-1}, as an off-white crystalline solid. The compound is known and its infrared and NMR data, given below, correspond to those reported for 2-(1H-benzimidazol-2-yl)phenol (CAS 2963-66-8, lit. m.p. 239–243 °C).

IR (KBr, cm^{-1}): 3417.63 (ν O–H, phenolic); 3209.33 (ν C–H, aromatic / ν N–H); 1612.38 (ν C=N); 1512.09 (ν C=C, aromatic); 1311.50 (ν C–O). ^{1}H NMR (DMSO-d_6, ppm): δ 10.84 (s, 1H, benzimidazole N–H), 8.15 (s, 1H, phenolic OH), 7.78–6.90 (m, 8H, aromatic H), 2.51 (DMSO-d_6). ^{13}C NMR (DMSO-d_6, ppm): δ 154 (C–OH), 152.9 (C-2 of the benzimidazole), 141 (ring-junction C), 132.2–115 (aromatic C), 40 (DMSO-d_6).

2.3. 1-(4-{[3-(1H-Benzimidazol-2-yl)-4-hydroxyphenyl]diazenyl}phenyl)ethan-1-one (2)

Diazotisation. 4-Aminoacetophenone (1.352 g, 10.0 mmol) was dissolved in a mixture of concentrated hydrochloric acid (3.0 mL, 11.7 M, 35 mmol, 3.5 equiv) and distilled water (10 mL), and the solution was cooled to 0–5 °C in an ice–salt bath. A pre-cooled solution of sodium nitrite (0.724 g, 10.5 mmol, 1.05 equiv) in distilled water (5 mL) was added dropwise over 15 min with vigorous stirring, the temperature being kept below 5 °C throughout, and the resulting pale-yellow diazonium solution was stirred for a further 30 min at 0–5 °C. A positive starch–iodide test confirmed the slight excess of nitrous acid, which was destroyed with a few crystals of urea immediately before coupling; the diazonium solution was used at once. Coupling. Compound 1 (2.102 g, 10.0 mmol, 1.00 equiv with respect to the diazonium salt) was dissolved in aqueous sodium hydroxide (10% w/v, 5.0 mL, 12.5 mmol, 1.25 equiv), the solution was diluted with distilled water to 25 mL and buffered to pH 9–10 with solid sodium carbonate, and it was cooled to 0–5 °C. A mildly alkaline medium is used in preference to a strongly alkaline one because aryldiazonium ions are converted above about pH 10 into the unreactive diazoate, while the phenol must still be present as the far more nucleophilic phenolate. The cold diazonium solution was added dropwise over 20 min with vigorous stirring, the temperature being held below 5 °C, and the deep red mixture was stirred for a further 2 h at 0–5 °C and then for 1 h as it warmed to room temperature. Azo coupling of a phenolate takes place preferentially at the position para to the hydroxyl group, and that position is unsubstituted in 1; this fixes the 1,3,4-substitution pattern given in the name of 2 [17]. The mixture was acidified to pH 5–6 with hydrochloric acid (10% v/v) and kept in the ice bath for 30 min. The precipitate was collected by suction filtration, washed with cold distilled water (5 × 25 mL) until the washings were neutral, dried at 60 °C and recrystallised from absolute ethanol to give 2, $C_{21}H_{16}N_4O_2$, M = 356.38 g mol^{-1}. Neutralisation of the alkaline coupling medium generates sodium chloride, and this step is the most likely origin of the traces of crystalline sodium chloride carried through to the sample examined by powder diffraction (Section 3.4).

IR (KBr, cm^{-1}): 3417 (ν O–H, phenolic); 1627.18 (ν C=O, ketone); 1599.09 (ν C=N); 1419.51 (ν N=N, azo). ^{1}H NMR (DMSO-d_6, ppm): δ 12.69 (s, 1H, benzimidazole N–H), 9.55 (s, 1H, phenolic OH), 8.50–6.50 (m, 11H, aromatic H), 2.51 (DMSO-d_6), 1.64 (s, 3H, $COCH_3$). ^{13}C NMR (DMSO-d_6, ppm): δ 195.68 (ketone C=O), 157.67, 154.62, 152.86, 145.28 (quaternary aromatic C), 141–115 (aromatic C), 39 (DMSO-d_6), 27.83 ($COCH_3$).

2.4. Ketimine precursor (9)

The azo ketone 2 (1.782 g, 5.0 mmol) and benzocaine (0.826 g, 5.0 mmol, 1.00 equiv) were dissolved in absolute ethanol (30 mL) in a 100 mL round-bottomed flask fitted with a reflux condenser carrying a calcium chloride guard tube, glacial acetic acid (5 drops, ca. 0.25 mL) was added as catalyst, and the equimolar mixture was heated under reflux at 78 °C with magnetic stirring for 10 h. Progress was followed by TLC (chloroform–methanol, 9:1, v/v) until the spot of 2 was no longer detectable. Condensation of a ketone with an aromatic amine is appreciably slower than that of an aldehyde, and the long reflux time reflects both the reduced electrophilicity and the greater steric demand of the acetyl carbonyl. The solution was concentrated to about one third of its volume under reduced pressure and kept overnight at 4 °C. The solid that separated was collected by filtration, washed with cold absolute ethanol (3 × 10 mL), dried under vacuum over anhydrous calcium chloride and recrystallised from absolute ethanol to give the ketimine 9, $C_{30}H_{25}N_5O_3$, M = 503.56 g mol^{-1}.

No spectra of the ketimine were available when this manuscript was prepared. Its identity rests on the elemental composition demanded by the mass balance of the cycloaddition (Section 3.1) and on the ^{13}C spectrum of 13, in which the ketone resonance of 2 at 195.68 ppm has gone and three carbonyl resonances have appeared in its place (Section 3.3).

2.5. Ethyl 4-[3-(4-{[3-(1H-benzimidazol-2-yl)-4-hydroxyphenyl]diazenyl}phenyl)-3-methyl-1,5-dioxo-1,5-dihydro-4H-benzo[e][1,3]oxazepin-4-yl]benzoate (13)

The ketimine 9 (0.5055 g, 1.004 mmol) and phthalic anhydride (0.1481 g, 1.000 mmol), an equimolar charge of 1.004:1.000, were dissolved in dry 1,4-dioxane (25 mL) in a 50 mL round-bottomed flask fitted with a reflux condenser carrying a calcium chloride guard tube, and the mixture was heated under reflux at 101 °C with magnetic stirring for 16 h [3, 4, 6]. Progress was followed by TLC (chloroform–methanol, 9:1, v/v) until the spot of 9 had disappeared. The dark red solution was cooled to room temperature and the solvent was removed under reduced pressure on a rotary evaporator at 45 °C. The residue was triturated with n-hexane (3 × 10 mL) to remove non-polar impurities, collected

by filtration, washed with cold distilled water (2 × 10 mL) to remove the phthalic acid formed from any unreacted anhydride, and with cold absolute ethanol (2 × 5 mL), and recrystallised from absolute ethanol to give the title compound, $C_{38}H_{29}N_5O_6$, M = 651.68 g mol^{-1}, as a red solid. Yield: 0.515 g (79%). m.p.: 280–282 °C. Rf: 0.60 (chloroform–methanol, 9:1, v/v).

IR (KBr, cm^{-1}): 3348.19 (ν O–H, phenolic, hydrogen-bonded); 3224.76, 3132.18 (ν N–H, benzimidazole); 3078.18 (ν C–H, aromatic); 2985.60, 2900.74 (ν C–H, aliphatic); 1712.67 (ν C=O, lactone); 1689.53 (ν C=O, lactam); 1596.95, 1542.95 (ν C=C, aromatic); 1411.80 (ν N=N, azo); 1280.65, 1242.07 (ν C–O, lactone and ester); 1172.64, 1110.92 (ν C–O / ν C–N); 1026.06, 887.19, 771.47, 702.04 (γ C–H, out-of-plane); 501.46 (skeletal). ^{1}H NMR (DMSO-d_6, ppm): δ 12.65 (s, benzimidazole N–H), 10.91 (s, 1H, phenolic OH), 7.95–7.62 (m, 8H, aromatic H), 6.58–6.34 (m, 4H, aromatic H), 4.31–4.18 (q, OCH_2), 3.57 (HDO), 2.52–2.50 (DMSO-d_6), 1.32–1.24 (CH_3 of the ethyl ester and CH_3 at C-3). ^{13}C NMR (DMSO-d_6, ppm): δ 167.03, 166.36, 165.78 (three C=O: lactone, lactam and ester), 153.87 (C–OH), 143.57, 137.24, 130.70, 130.66, 125.08, 119.29, 116.49, 113.12 (aromatic C), 59.94 (OCH_2), 40.55–39.30 (DMSO-d_6), 27.26 (CH_3 at C-3), 14.66 (CH_3 of the ethyl ester). Anal. calcd for $C_{38}H_{29}N_5O_6$: C 70.04, H 4.49, N 10.75. HRMS (ESI+, m/z): calcd for $C_{38}H_{30}N_5O_6$ $[M+H]^+$ 652.2191. Canonical SMILES: CCOC(=O)c1ccc(cc1)N1C(=O)c2ccccc2C(=O)OC1(C)c1ccc(cc1)N=Nc1ccc(O)c(c1)-c1nc2ccccc2[nH]1.

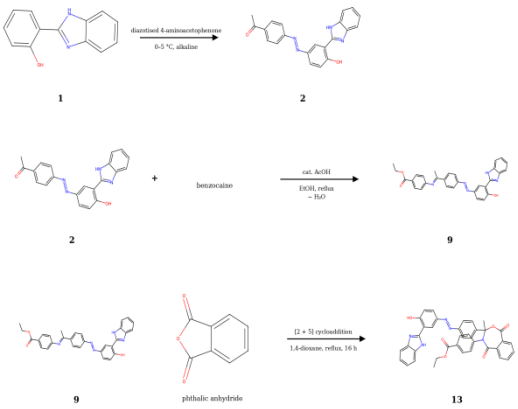

Figure 01: Four-step route to compound 13. The final step is the [2+5] cycloaddition of phthalic anhydride across the ketimine of 9.

2.6. Computational details

All density-functional calculations were performed with the PySCF program package [24]. The three-dimensional structure of 13 was generated from the canonical SMILES string given in Section 2.5 with the ETKDGv3 distance-geometry algorithm as implemented in RDKit; forty conformers were requested (random seed 42, RMSD pruning threshold 0.6 Å) and relaxed with the MMFF94 force field, and the lowest-energy structures were then fully optimised with the semi-empirical tight-binding method GFN2-xTB [25] as implemented in the tblite library, using an analytic-gradient L-BFGS minimisation.

An analytic B3LYP/6-31G(d) Hessian, and therefore a vibrationally verified B3LYP geometry optimisation, was beyond the computing budget available for the present study: the molecule contains 78 atoms and requires more than seven hundred contracted Gaussian functions, so a full DFT optimisation followed by an analytic second-derivative calculation was not attainable. The protocol adopted instead, and used consistently throughout this work, is B3LYP/6-31G(d)//GFN2-xTB: the geometry, the harmonic frequencies and the rigid-rotor/harmonic-oscillator thermochemical corrections are obtained at the GFN2-xTB level, and the electronic structure-orbital energies, conceptual-DFT descriptors, electrostatic potential and atomic charges-is obtained from a B3LYP/6-31G(d) single-point calculation at that geometry. All wavenumbers and thermochemical values reported below are therefore semi-empirical and are quoted unscaled.

Global reactivity descriptors were obtained from the frontier-orbital energies within Koopmans' approximation: $I = -E(HOMO)$, $A = -E(LUMO)$, electronegativity $\chi = (I + A)/2$, chemical potential $\mu = -\chi$, chemical hardness $\eta = (I - A)/2$, global softness $\sigma = 1/(2\eta)$, electrophilicity index $\omega = \mu^2/(2\eta)$ and maximum charge transfer $\Delta N_{max} = -\mu/\eta$. The nucleophilicity index N was computed as $N = E(HOMO) - E(HOMO)_{TCE}$ with E(HOMO)TCE = −9.12 eV (−0.3351 a.u.), the value that underlies the original definition of Domingo [26]; the classification thresholds are those calibrated at B3LYP/6-31G(d) in the gas phase, that is, at the same level of theory used here [27]. The molecular electrostatic potential was computed from the converged first-order density matrix and evaluated on the ρ = 0.001 a.u. electron-density isosurface, and atomic charges were obtained from Mulliken and meta-Löwdin population analyses.

Condensed Fukui functions were obtained from single-point calculations on the N-, (N + 1)- and (N − 1)-electron systems at the optimised geometry of the neutral molecule, using the Mulliken charges q of the three species: $f^+ = q(N) - q(N + 1)$ for nucleophilic attack and $f^- = q(N - 1) - q(N)$ for electrophilic attack. The dual descriptor is $\Delta f = f^+ - f^-$, a positive value marking an electrophilic and a negative value a nucleophilic site, and the local softnesses are $s^+ = \sigma f^+$ and $s^- = \sigma f^-$ with the global softness σ defined above.

2.7. Cytotoxicity assay

Cell lines and culture. The HepG2 human hepatocellular carcinoma line and the WRL-68 normal human embryonic hepatocyte line were obtained from the cell-bank collection of the Iraqi Center for Cancer and Medical Genetic Research (ICCMGR), Mustansiriyah University, Baghdad, Iraq. Both lines were maintained in RPMI-1640 medium supplemented with 10% (v/v) heat-inactivated foetal bovine serum, 100 U mL^{-1} penicillin

and 100 µg mL⁻¹ streptomycin, and were grown at 37 °C in a humidified incubator under 5% CO_2. Cells in the exponential growth phase were harvested with 0.25% trypsin–EDTA and counted in a haemocytometer by trypan-blue exclusion; only suspensions of viability above 95% were used. Both are established, commercially available cell lines and no primary human material was used, so no ethical approval was required.

Treatment. Cells were seeded into flat-bottomed 96-well microtitre plates at 1 × 10^4 cells per well in 200 µL of complete medium and left to attach for 24 h at 37 °C. A stock solution of 13 (40 mg mL⁻¹) was prepared in dimethyl sulfoxide and diluted with serum-free medium to give seven serial concentrations of 400, 200, 100, 50, 25, 12.5 and 6.20 µg mL⁻¹, which correspond to 614, 307, 153, 76.7, 38.4, 19.2 and 9.5 µM for a molecular weight of 651.68 g mol⁻¹. The dimethyl sulfoxide content of the wells was therefore 1.0% (v/v) at the highest concentration and proportionally lower at every other concentration. The culture medium was then replaced with 200 µL of the appropriate dilution and the plates were incubated for a further 24 h at 37 °C under 5% CO_2. Untreated cells receiving medium containing 1.0% (v/v) dimethyl sulfoxide served as the vehicle control and wells containing medium alone as the blank. Each concentration was applied to three replicate wells and the experiment was repeated three times independently.

MTT step. After exposure the treatment medium was removed and each well was washed with phosphate-buffered saline (pH 7.4). MTT [3-(4,5-dimethylthiazol-2-yl)-2,5-diphenyltetrazolium bromide] solution (2 mg mL⁻¹ in phosphate-buffered saline, 28 µL) and serum-free medium (150 µL) were added to every well and the plates were incubated in the dark for 2.5 h at 37 °C [28]. The supernatant was then discarded and the purple formazan was dissolved in dimethyl sulfoxide (130 µL) with gentle shaking for 15 min at 37 °C. Absorbance was measured at 492 nm, with 630 nm as the reference wavelength, on a Bio-Rad iMark microplate reader (Bio-Rad Laboratories, Hercules, CA, USA).

Data treatment. Viability was calculated as the absorbance of the treated wells, corrected for the blank, divided by the absorbance of the vehicle control wells, corrected in the same way, and multiplied by 100; growth inhibition is 100 minus the viability. Half-maximal inhibitory concentrations were obtained by fitting the mean viability against the logarithm of the concentration to a four-parameter logistic function with a variable Hill slope; where 50% inhibition was not reached within the range tested, the IC_{50} is reported as a bound rather than as an interpolated value. The selectivity index was defined as the ratio of the IC_{50} against WRL-68 to the IC_{50} against HepG2, and, because neither value could be interpolated within the range studied, it is likewise reported here only as a bound. Results are reported as means of three independent experiments; differences between the two cell lines at each concentration were assessed by an unpaired two-tailed Student's t-test, and $p < 0.05$ was taken as significant.

3. RESULTS AND DISCUSSION

3.1. Synthesis

The four steps proceed as the literature on related systems would suggest (Fig. 1). Condensation of o-phenylenediamine with salicylaldehyde gives the benzimidazolyl phenol 1; diazotised 4-aminoacetophenone couples with the activated position of the phenol ring to give the azo ketone 2; and condensation of that ketone with benzocaine under acid catalysis gives the ketimine 9. The final step is the [2+5] cycloaddition of phthalic anhydride across the C=N bond of 9 in refluxing 1,4-dioxane. Mechanistically the imine nitrogen attacks one of the two anhydride carbonyl carbons, and the carboxylate generated by opening of the five-membered anhydride ring then closes onto the former imine carbon, so that one anhydride carbonyl becomes the lactam carbonyl C-5 and the other becomes the lactone carbonyl C-1 of the seven-membered ring.

Three features of this step are worth emphasising because they provide an internal check on the product assignment. First, no small molecule is expelled, so the product must be the simple 1:1 adduct: 503.56 g mol⁻¹ for the ketimine 9 ($C_{30}H_{25}N_5O_3$) plus 148.12 g mol⁻¹ for phthalic anhydride gives 651.68 g mol⁻¹ for $C_{38}H_{29}N_5O_6$, exactly the molecular weight assigned to 13. Second, the quantities used, 0.5055 g of 9 and 0.1481 g of phthalic anhydride, correspond to 1.004 and 1.000 mmol respectively, an equimolar charge to within half a percent. Third, because the carbonyl partner in the third step is a ketone rather than an aldehyde, the resulting ring carbon C-3 is fully substituted: it carries a methyl group, the aryl group of the azo fragment, the ring oxygen and the ring nitrogen. This quaternary N,O-acetal centre is the structural feature that distinguishes the present compound from the more common aldehyde-derived benzoxazepines, and it has direct consequences for the NMR spectrum discussed in Section 3.3.

It should be noted that the systematic name recorded for 13 in the primary laboratory record describes the central phenylene ring as meta-substituted, whereas the azo coupling of a diazonium salt derived from 4-aminoacetophenone necessarily places the acetyl group para to the azo linkage, as drawn in Fig. 1 and as the name of the precursor 2 requires. The para connectivity is used consistently throughout this work; the molecular formula and molecular weight are unaffected by the choice.

3.2. Infrared spectra

The infrared spectrum of 1 shows the phenolic O–H stretch at 3417.63 cm⁻¹, the C=N stretch of the benzimidazole ring at 1612.38 cm⁻¹, aromatic C=C stretching at 1512.09 cm⁻¹ and the C–O stretch at 1311.50 cm⁻¹. After azo coupling, the spectrum of 2 retains the phenolic O–H and the benzimidazole C=N at 1599.09 cm⁻¹, and adds two new features that identify the frag-

ment introduced: the acetyl carbonyl at 1627.18 cm^{-1} and the azo N=N stretch at 1419.51 cm^{-1}.

The spectrum of the benzoxazepine 13 (Fig. 2) is the most informative of the series. The single carbonyl band of the precursor is replaced by two, a strong absorption at 1712.67 cm^{-1} assigned to the lactone carbonyl C-1 of the new ring and a second at 1689.53 cm^{-1} assigned to the lactam carbonyl C-5. A separation of 23 cm^{-1} between them is what one expects when an ester-type and an amide-type carbonyl are placed on the same seven-membered ring: the lactam carbonyl is lowered by amide resonance, in which the nitrogen lone pair is delocalised onto the carbonyl oxygen and the C=O bond order is correspondingly reduced, whereas the lactone carbonyl retains a higher force constant because the ring oxygen is a much weaker π donor. The ester carbonyl of the benzoate fragment takes no part in the reaction and is not resolved from the lactone band; both fall inside the strong envelope centred at 1712.67 cm^{-1}.

Three further observations confirm that the rest of the molecule survives the cycloaddition intact. The azo N=N stretch is retained, moving only from 1419.51 cm^{-1} in 2 to 1411.80 cm^{-1} in 13, so the chromophore is undisturbed — consistent with the red colour of the product. The benzimidazole N–H stretches appear at 3224.76 and 3132.18 cm^{-1}; the benzimidazole C=N stretch, at 1612.38 cm^{-1} in 1 and 1599.09 cm^{-1} in 2, is not separately resolved in 13 because it lies beneath the strong aromatic C=C envelope centred at 1596.95 cm^{-1}. and the phenolic O–H gives a broad band at 3348.19 cm^{-1}, lower than the 3417.63 cm^{-1} of the parent phenol, which indicates stronger hydrogen bonding in the solid once three carbonyl acceptors are available. Aliphatic C–H stretches at 2985.60 and 2900.74 cm^{-1} belong to the ethyl ester and to the methyl group installed at C-3, and the out-of-plane deformations at 771.47 and 702.04 cm^{-1} are characteristic of the ortho-disubstituted ring of the phthaloyl fragment. All measured bands are collected in Table 1.

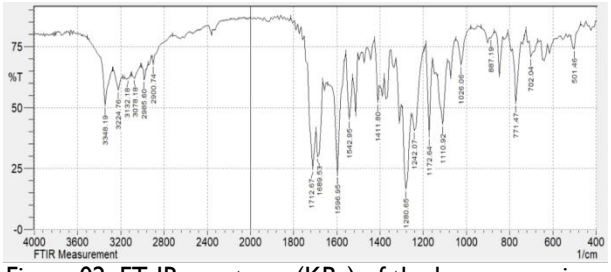

Figure 02: FT-IR spectrum (KBr) of the benzoxazepine 13.

Table 01: Characteristic infrared bands of compounds 1, 2 and 13 (KBr, cm^{-1}).

Assignment	1	2	13
ν(O–H) phenolic	3417.63	3417	3348.19
ν(N–H) benzimidazole	3209.33	—	3224.76, 3132.18
ν(C–H) aromatic	3209.33	—	3078.18
ν(C–H) aliphatic	—	—	2985.60, 2900.74
ν(C=O) lactone (ring C-1)	—	—	1712.67
ν(C=O) lactam (ring C-5)	—	—	1689.53
ν(C=O) ketone	—	1627.18	—
ν(C=N) benzimidazole	1612.38	1599.09	not resolved
ν(C=C) aromatic	1512.09	—	1596.95, 1542.95
ν(N=N) azo	—	1419.51	1411.80
ν(C–O)	1311.50	—	1280.65, 1242.07
ν(C–O) / ν(C–N)	—	—	1172.64, 1110.92
γ(C–H) out-of-plane	—	—	1026.06, 887.19, 771.47, 702.04
skeletal	—	—	501.46

3.3. NMR spectra

The ^{1}H spectrum of the benzimidazolyl phenol 1 shows the benzimidazole N–H at 10.84 ppm, the phenolic hydroxyl at 8.15 ppm and eight aromatic protons between 7.78 and 6.90 ppm. Its ^{13}C spectrum places the phenolic carbon at 154 ppm, the C-2 carbon of the benzimidazole ring at 152.9 ppm and the remaining aromatic carbons between 132.2 and 115 ppm. After azo coupling the ^{1}H spectrum of 2 shifts the N–H to 12.69 ppm and the hydroxyl to 9.55 ppm, both consistent with the stronger electron withdrawal exerted by the azo group, and adds a three-proton acetyl singlet at 1.64 ppm; the ^{13}C spectrum shows the ketone carbonyl at 195.68 ppm and the acetyl methyl at 27.83 ppm.

In the ^{1}H spectrum of 13 (Fig. 3) the benzimidazole N–H is still present as a weak singlet at 12.65 ppm and the phenolic hydroxyl at 10.91 ppm; aromatic multiplets occupy the 7.95–7.62 and 6.58–6.34 ppm windows, the ester quartet appears between 4.31 and 4.18 ppm, and the region between 1.32 and 1.24 ppm contains both the triplet of the ethyl ester and the singlet of the methyl group at C-3. Full data for all three compounds are collected in Table 2.

The ^{13}C spectrum of 13 (Fig. 4) provides the clearest single piece of evidence for the new ring. Three carbonyl resonances appear at 167.03, 166.36 and 165.78 ppm, whereas the precursor 9 carries only the ester carbonyl of the benzoate fragment; the two additional signals are the lactone and lactam carbonyls generated by opening of the anhydride. The ketone carbonyl of 2 at 195.68 ppm has disappeared completely, which shows that the carbonyl was consumed in forming the ketimine and is no longer present as a ketone. The

methyl group now attached to the ring carbon C-3 resonates at 27.26 ppm and the ethyl ester gives its OCH_2 carbon at 59.94 ppm and its methyl at 14.66 ppm. The phenolic carbon appears at 153.87 ppm and the remaining aromatic carbons fall between 143.57 and 113.12 ppm.

Two points must be stated plainly rather than glossed over. The first concerns the quaternary ring carbon C-3. In an aldehyde-derived benzoxazepine this position is a methine and is normally observed between 80 and 90 ppm; here it carries no hydrogen at all, being substituted by a methyl group, an aryl group, the ring oxygen and the ring nitrogen. No resonance is observed anywhere between 65 and 113 ppm in the spectrum recorded here. A fully substituted carbon of this kind has a long spin–lattice relaxation time and receives no nuclear Overhauser enhancement, so its absence from a routine proton-decoupled ^{13}C spectrum acquired with a short relaxation delay is expected rather than surprising; the same is not true of a methine. Nevertheless, direct observation of C-3 would place the structure beyond doubt, and a ^{13}C spectrum recorded with a substantially longer relaxation delay and a larger number of transients, or an HMBC experiment correlating the C-3 carbon with the methyl protons at 1.3 ppm, is recommended before the structure is regarded as fully proven.

The second point concerns the integrals. The molecular formula requires nineteen aromatic protons distributed over five rings, together with one N–H, one O–H, one OCH_2 and two CH_3 groups. The integrals measured on the spectrum reproduced in Fig. 3 account for roughly twelve aromatic protons, and the ^{13}C spectrum resolves nine distinct aromatic carbons where a molecule of this size would be expected to show considerably more even after allowing for the local two-fold symmetry of the two para-disubstituted rings. Signal overlap in the crowded aromatic region, the low solubility of a compound melting above 280 °C, and residual solvent are all plausible contributors. A spectrum recorded on a more concentrated sample, or at higher field, would resolve the question, and elemental analysis and high-resolution mass spectrometry — for which the calculated values are given in Section 2.5 — would confirm the composition independently.

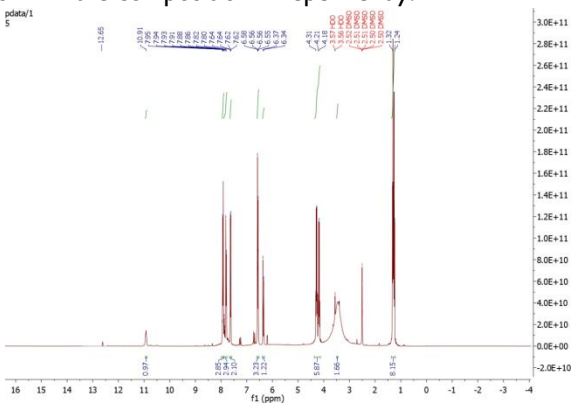

Figure 03: ^{1}H NMR spectrum (DMSO-d_6) of the benzoxazepine 13.

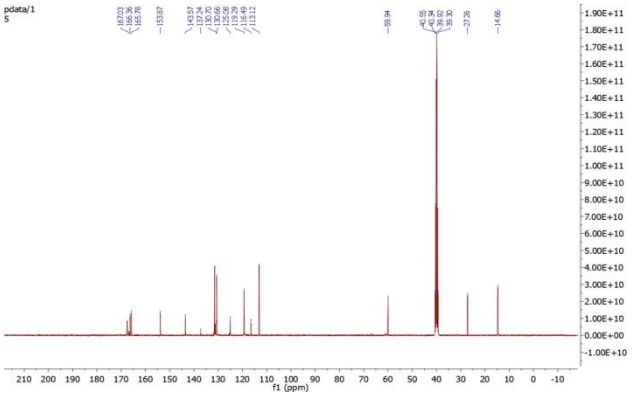

Figure 04: ^{13}C NMR spectrum (DMSO-d_6) of the benzoxazepine 13. The three carbonyl resonances at 167.03, 166.36 and 165.78 ppm are the signature of the new ring.

Table 02: ^{1}H and ^{13}C NMR data for compounds 1, 2 and 13 (DMSO-d_6, chemical shifts in ppm).

Cmpd	Nucleus	δ (ppm)	Mult.	Assignment
1	^{1}H	10.84	s	benzimidazole N–H
1	^{1}H	8.15	s	phenolic O–H
1	^{1}H	7.78–6.90	m	aromatic H (8H)
1	^{13}C	154	—	C–OH
1	^{13}C	152.9	—	C-2, benzimidazole
1	^{13}C	141	—	ring-junction C
1	^{13}C	132.2–115	—	aromatic C
2	^{1}H	12.69	s	benzimidazole N–H
2	^{1}H	9.55	s	phenolic O–H
2	^{1}H	8.50–6.50	m	aromatic H (11H)
2	^{1}H	1.64	s	$COCH_3$
2	^{13}C	195.68	—	ketone C=O
2	^{13}C	157.67, 154.62, 152.86, 145.28	—	quaternary aromatic C
2	^{13}C	141–115	—	aromatic C
2	^{13}C	27.83	—	$COCH_3$
13	^{1}H	12.65	s	benzimidazole N–H
13	^{1}H	10.91	s	phenolic O–H

Cmpd	Nucleus	δ (ppm)	Mult.	Assignment
13	^{1}H	7.95–7.62	m	aromatic H
13	^{1}H	6.58–6.34	m	aromatic H
13	^{1}H	4.31–4.18	q	OCH_2
13	^{1}H	1.32–1.24	t + s	CH_3 (ester) and CH_3 at C-3
13	^{13}C	167.03, 166.36, 165.78	—	three C=O: lactone, lactam, ester
13	^{13}C	153.87	—	C–OH
13	^{13}C	143.57–113.12	—	aromatic C
13	^{13}C	59.94	—	OCH_2
13	^{13}C	27.26	—	CH_3 at C-3
13	^{13}C	14.66	—	CH_3 of the ethyl ester
13	^{13}C	not observed	—	C-3, quaternary N,O-acetal (see text)

3.4. Powder X-ray diffraction

The diffraction pattern (Fig. 5) is dominated by a broad, featureless halo centred at 2θ = 24.6°, corresponding to a Bragg spacing of 3.62 Å and a full width at half maximum of about 5.6°. A halo at this position is the standard signature of an X-ray-amorphous aromatic organic solid, the 3.6 Å spacing being the mean separation between π-stacked aryl rings. Its presence establishes that the bulk of the material has no long-range order, which is unremarkable for a large, flexible, multiply substituted molecule precipitated from solution and is consistent with the broad melting range recorded for the compound.

Superimposed on this halo is a small set of sharp reflections at 2θ = 31.72, 45.44, 56.48, 66.24 and 75.28°. Their spacings, 2.819, 1.994, 1.628, 1.410 and 1.261 Å, index without residue as the (200), (220), (222), (400) and (420) reflections of face-centred cubic sodium chloride; the measured (200) spacing of 2.819 Å differs from the reference value of 2.821 Å by 0.07%. Applying the Scherrer equation with a shape factor of 0.9 to the four strongest of these reflections gives crystallite sizes of 32.7, 31.5, 29.8 and 24.4 nm, a mean of 29.6 nm; the indexing and the Scherrer analysis are collected in Table 3. The salt is a residue of the workup rather than a component of the product, and its presence is a purity observation rather than a structural one: it indicates that the sample submitted for diffraction had not been washed free of inorganic material. Removing it by washing the solid with water before drying, or by recrystallisation from a solvent in which sodium chloride is insoluble, would give a cleaner pattern; the amorphous halo, however, would remain, since it reflects the intrinsic packing of the organic phase.

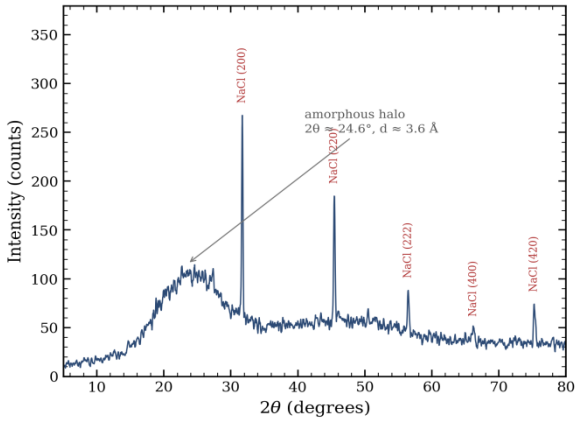

Figure 05: Powder X-ray diffraction pattern (Cu Kα₁, λ = 1.5406 Å). The broad halo at 2θ ≈ 24.6° is the amorphous organic phase; the sharp reflections are residual crystalline sodium chloride.

Table 03: Sharp reflections in the diffraction pattern, indexed as face-centred cubic sodium chloride, with Scherrer crystallite sizes (K = 0.9).

2θ (°)	d (Å)	Rel. int. (%)	FWHM (°)	hkl	D (nm)
31.72	2.819	100	0.252	(200)	32.7
45.44	1.994	69	0.273	(220)	31.5
56.48	1.628	33	0.303	(222)	29.8
66.24	1.410	14	—	(400)	—
75.28	1.261	28	0.412	(420)	24.4
halo, 24.6	3.62	43	≈5.6	amorphous	—

3.5. Calculated vibrational spectrum

Table 4 compares the measured wavenumbers of 13 with those calculated from the semi-empirical Hessian. The agreement over the fingerprint region is good: across the eleven bands between 1750 and 700 cm^{-1} that are not affected by hydrogen bonding or by strong mode coupling — that is, excluding the two X–H stretches and the azo stretch discussed below — the mean absolute deviation is 12 cm^{-1} with an RMSD of 17 cm^{-1}, and the region that matters most for the structural argument is reproduced almost exactly. The calculation places the lactone stretch at 1712.2 cm^{-1} against a measured 1712.67 cm^{-1} and the lactam stretch at 1691.4 cm^{-1} against a measured 1689.53 cm^{-1}, deviations of 0.5 and 1.9 cm^{-1} respectively, and it predicts a third carbonyl mode at 1740.9 cm^{-1} for the benzoate ester. That third band is not resolved experimentally, which is exactly what the calculation implies: the ester and lactone modes lie 29 cm^{-1} apart and merge into the single strong envelope observed at 1712.67 cm^{-1}, while the lactam mode, lowered by amide resonance, separates cleanly. The independent re-

production of the carbonyl pattern is the strongest computational support for the assigned ring structure.

Two calculated bands deviate strongly and both deviations are informative rather than troubling. The benzimidazole N–H stretch is calculated at 3380.3 cm^{-1} but measured at 3224.76 cm^{-1}, and the phenolic O–H is calculated at 2830.7 cm^{-1} but measured as a broad band at 3348.19 cm^{-1}; the gas-phase calculation describes an isolated molecule in which the phenol is locked into a strong intramolecular hydrogen bond and the N–H is free, whereas in the KBr disc both groups participate in an intermolecular network that redistributes the two frequencies. The intramolecular contact itself is a real and chemically important feature of the optimised structure and is discussed in Section 3.6. The azo stretch is the second outlier, calculated at 1516.7 cm^{-1} against a measured 1411.80 cm^{-1}. Azo stretching is strongly coupled to the ring modes of the two aryl groups it joins, so its position is sensitive to the description of that coupling, and a semi-empirical Hessian is not expected to reproduce it well; the band is nonetheless clearly present in both the calculated and the measured spectrum, and its retention from the precursor is what matters for the structural argument.

Table 04: Measured infrared wavenumbers of compound 13 (KBr, cm^{-1}) compared with the calculated harmonic values (GFN2-xTB, unscaled).

Assignment	Experimental	Calculated	Calc. – exp.
ν(O–H) phenolic, intramolecularly bonded	3348.19	2830.7	—
ν(N–H) benzimidazole	3224.76	3380.3	+155.5
ν(C=O) ester	1712.67 (envelope)	1740.9	+28.2
ν(C=O) lactone	1712.67 (s)	1712.2	-0.5
ν(C=O) lactam	1689.53 (m)	1691.4	+1.9
ν(C=C) aromatic	1596.95	1599.3	+2.3
ν(C=C) aromatic	1542.95	1537.2	-5.8
ν(N=N) azo (coupled with ring modes)	1411.80	1516.7	+104.9
ν(C–O) lactone / ester	1280.65	1275.9	-4.8
ν(C–O)	1242.07	1238.4	-3.7
ν(C–O) / ν(C–N)	1110.92	1128.2	+17.3
ring / C–O	1026.06	1064.0	+37.9
γ(C–H) out-of-plane	771.47	782.5	+11.0
γ(C–H) ortho-benzo	702.04	681.2	-20.8

The O–H entry carries no deviation because the calculated and measured bands describe different hydrogen-bonding situations, as explained above; it is excluded from the statistics quoted in the text.

The full calculated infrared spectrum, constructed by dressing each harmonic stick with a Lorentzian profile of 8 cm^{-1} half-width, is shown in Fig. 6. Three carbonyl bands dominate the 1600–1800 cm^{-1} window — the benzoate ester at 1741 cm^{-1}, the lactone at 1712 cm^{-1} and the lactam at 1691 cm^{-1} — and the azo stretch appears as a clearly resolved peak at 1517 cm^{-1}. The most intense band in the entire spectrum falls near 1300 cm^{-1} and corresponds to mixed C–O and C–N stretching modes of the seven-membered ring and the ester linkages, consistent with the cluster of strong absorptions at 1280–1170 cm^{-1} in the experimental spectrum.

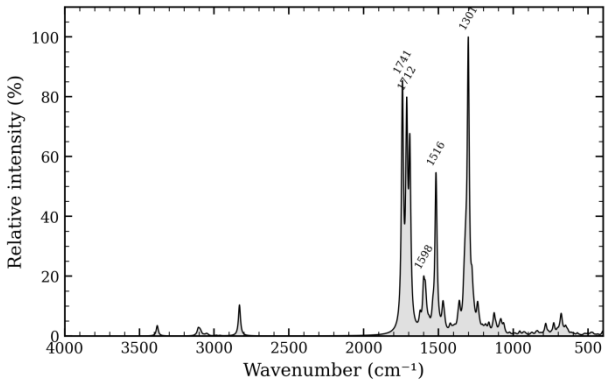

Figure 06: Calculated infrared spectrum of compound 13 (GFN2-xTB harmonic frequencies, unscaled, Lorentzian broadening with γ = 8 cm^{-1}).

3.6. Optimised geometry and frontier molecular orbitals

The molecule was relaxed at the GFN2-xTB level from a conformer search over forty ETKDG-generated structures, and the electronic structure was then obtained from a B3LYP/6-31G(d) single-point calculation at that geometry using 744 contracted Gaussian functions for the 78 atoms. The harmonic analysis returns 228 real vibrational modes and no imaginary frequency, which establishes that the structure discussed here is a genuine minimum on the semi-empirical potential-energy surface.

The optimised structure is shown in Fig. 07. The molecule is built from five aromatic rings-the benzimidazole, the phenol ring that carries it, the central phenylene of the azo bridge, the fused benzo ring of the phthaloyl unit, and the benzoate ring on nitrogen-arranged around a single seven-membered heterocycle. The qua-

ternary carbon C-3 is the only sp^3 centre in the framework and, carrying four different substituents, it is a stereogenic centre; because none of the reagents is chiral the product is obtained as a racemate, so that every scalar property reported here is identical for the two enantiomers even though an interaction with a chiral biological target would not be.

The frontier orbitals are shown in Fig. 8 and their energies are collected in Table 5. The HOMO lies at -5.523 eV and the LUMO at -1.931 eV, giving a gap of 3.592 eV. Partitioning the Mulliken population of each frontier orbital over the molecular fragments makes the description quantitative: the HOMO is concentrated on the benzimidazolyl phenol donor (benzimidazole 62.3%, phenol ring 24.0%), while the LUMO is carried by the azo bridge together with the central phenylene and the phthaloyl acceptor. The azo bridge alone carries 51% of the LUMO. The azo linkage is the decisive structural element here: unlike the sp^3 carbon that interrupts conjugation between the two halves of a simple aldehyde-derived benzoxazepine, the N=N bridge is planar and fully conjugating, so it ties the benzimidazolyl phenol donor to the rest of the π system. That is why the gap of 3.592 eV is substantially narrower than the 3.90–4.80 eV reported at B3LYP/6-31G(d,p) for benzimidazole-tethered oxazepines that lack an azo bridge [23], and it is also the reason the compound is intensely coloured, the red of the solid being the visible-region tail of the resulting charge-transfer absorption.

One feature of the optimised structure deserves separate mention because it explains several of the spectroscopic observations at once. The phenolic hydroxyl and the pyridine-type nitrogen of the benzimidazole ring are held in a six-membered arrangement by a strong intramolecular hydrogen bond: the H···N distance is 1.690 Å with an O–H···N angle of 148°, and the O–H bond is stretched to 0.998 Å from its normal 0.96 Å. A contact this short is a resonance-assisted hydrogen bond, the geometry characteristic of 2-(benzimidazol-2-yl)phenols, and it accounts for the very low calculated O–H stretching wavenumber discussed in Section 3.5, for the breadth of the measured O–H band, and for the unusually downfield position of the hydroxyl proton at 10.91 ppm. It also means that the phenol is not freely available as a hydrogen-bond donor to an external acceptor, which is relevant to any later discussion of binding or of hydrogen-atom transfer.

Selected calculated bond lengths are collected in Table 6. The three carbonyl distances are 1.2141 Å for the lactone, 1.2146 Å for the lactam and 1.2027 Å for the benzoate ester; the azo bond at 1.2633 Å is a normal N=N double bond for a trans-azoarene, confirming that the chromophore is intact. At the quaternary ring carbon the C–O distance is 1.4271 Å and the C–N distance 1.4579 Å, both long single bonds as expected for an N,O-acetal centre bearing four substituents.

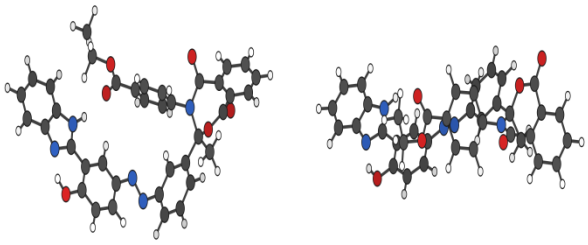

Figure 07: GFN2-xTB optimised structure of compound 13 in two orthogonal orientations. Carbon grey, hydrogen white, nitrogen blue, oxygen red.

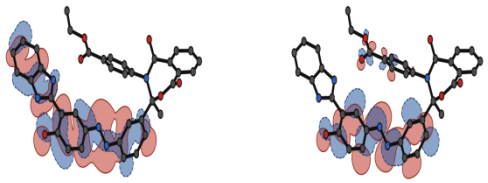

Figure 08: Isosurface plots (±0.02 a.u.) of the HOMO and the LUMO of compound 13.

Table 05: Frontier-orbital energies and conceptual-DFT global reactivity descriptors at B3LYP/6-31G(d)//GFN2-xTB.

Quantity	Symbol	Value	Unit
Energy of the HOMO	E(HOMO)	-5.5228	eV
Energy of the LUMO	E(LUMO)	-1.9312	eV
Energy of HOMO−1	E(HOMO−1)	-5.9038	eV
Energy of LUMO+1	E(LUMO+1)	-1.7437	eV
Energy gap	ΔE	3.5916	eV
Ionisation potential	I	5.5228	eV
Electron affinity	A	1.9312	eV
Electronegativity	χ	3.7270	eV
Chemical potential	μ	-3.7270	eV
Chemical hardness	η	1.7958	eV
Global softness	σ	0.2784	eV^{-1}
Electrophilicity index	ω	3.8675	eV
Nucleophilicity index	N	3.5972	eV
Maximum charge transfer	ΔN_{max}	2.0754	—

Quantity	Symbol	Value	Unit
Dipole moment	μ_{el}	3.6009	Debye
Total electronic energy	E	-2190.57538	Hartree
Number of basis functions	—	744	—

Table 06: Selected calculated bond lengths (Å) and the intramolecular hydrogen-bond geometry of compound 13 (GFN2-xTB).

Parameter	Calculated value
C=O, lactone (ring C-1)	1.2141 Å
C=O, lactam (ring C-5)	1.2146 Å
C=O, benzoate ester	1.2027 Å
N=N, azo bridge	1.2633 Å
C-3–O, ring (N,O-acetal)	1.4271 Å
C-3–N, ring (N,O-acetal)	1.4579 Å
O–H, phenolic	0.9978 Å
H···N, intramolecular	1.6899 Å
O–H···N angle	147.7°

The frontier-orbital energies are displayed as an energy-level diagram in Fig. 9, which shows the ten orbitals nearest to the gap. The occupied manifold is dense-HOMO to HOMO−4 span barely 1.1 eV-reflecting the extended π system and the availability of many nearly degenerate lone-pair combinations. The virtual manifold is somewhat broader, with the five lowest unoccupied orbitals spread over about 0.9 eV. The HOMO–LUMO gap of 3.592 eV sits between two groups of closely spaced levels and is by far the largest energy jump in this region, which justifies the use of Koopmans-based descriptors.

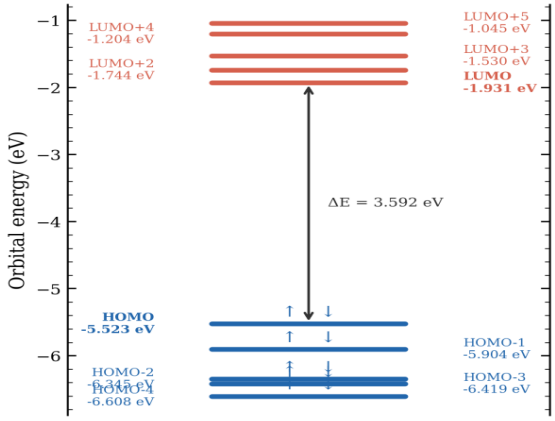

Figure 09: Frontier-orbital energy-level diagram of compound 13 at B3LYP/6-31G(d)//GFN2-xTB. Occupied levels in blue, virtual in red; spin pairing shown with arrows.

The Gaussian-broadened density of states (Fig. 10, σ = 0.15 eV) gives a complementary view: the occupied band extends from about −10.5 to −5.5 eV with its highest peak near −10 eV, where the deep-lying σ framework of five aromatic rings piles up. A clear gap separates it from the virtual band, whose leading edge starts at the LUMO position (−1.931 eV). The asymmetry between the two band widths — the occupied band is roughly twice as wide as the virtual band in the window shown — is a natural consequence of the large number of σ and lone-pair orbitals that contribute only to the occupied side.

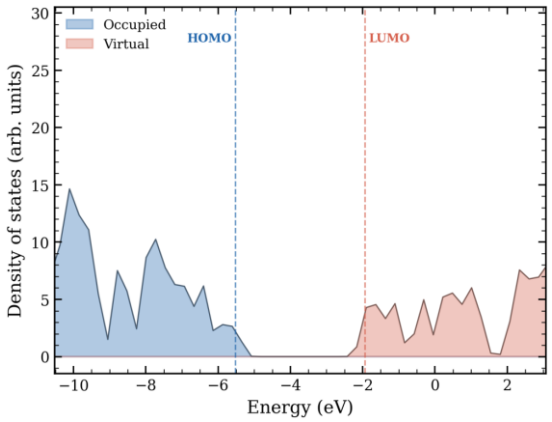

Figure 10: Density of states of compound 13 (Gaussian broadening, σ = 0.15 eV). Dashed vertical lines mark the HOMO and LUMO positions.

3.7. Global reactivity descriptors and electrostatic potential

The ionisation potential of 5.523 eV and the electron affinity of 1.931 eV give an electronegativity of 3.727 eV, a chemical hardness of 1.796 eV and a global softness of 0.278 eV^{-1}. The electrophilicity index ω = 3.867 eV places the compound in the strong-electrophile range (ω > 1.5 eV) on the scale of Domingo, Ríos-Gutiérrez and Pérez [26] calibrated at the same level of theory used here [27], and the nucleophilicity index N = 3.597 eV places it in the strong-nucleophile range (N > 3.0 eV). The comparison with azo-free benzimidazole–oxazepine hybrids is instructive: gaps of 3.90–4.80 eV have been reported for that family at a comparable B3LYP level [23], which within the same Koopmans approximation correspond to chemical hardness values of 1.95–2.40 eV, so the 1.796 eV found here lies below the whole azo-free range. Extending the conjugation through the azo bridge therefore makes the present compound the softer of the two and, at a comparable electronegativity, the more electrophilic. Softness of this kind is often invoked in discussions of biological activity, since a soft, polarisable molecule interacts more readily with the soft nucleophilic centres of proteins and nucleic acids [29–31], and the modest but reproducible selectivity for the tumour line reported in Section 3.10 is consistent with that picture.

The electrostatic potential mapped on the ρ = 0.001 a.u. isodensity surface (Fig. 11) runs from -35.9 to +23.6 kcal mol^{-1}. The negative regions are concentrated over the carbonyl oxygens of the seven-membered ring and the ester, which are the sites where a proton, a metal ion or a hydrogen-bond donor would attach first, together with the pyridine-type ni-

trogen of the benzimidazole and the lone pairs of the azo group. The most positive region of the whole surface, however, is not the phenolic hydrogen but the benzimidazole N–H, and the reason is the intramolecular hydrogen bond described above: because the phenolic proton is already engaged with the benzimidazole nitrogen, the N–H of the same ring is left as the only fully exposed donor and becomes the point of strongest positive potential. The deepest minimum sits over the carbonyl oxygen of the benzoate ester, with the lactone and lactam oxygens of the seven-membered ring close behind. A molecule presenting this combination — several strong acceptors on one face, two donors on the other, and a large hydrophobic surface from five aromatic rings — has the hydrogen-bonding vocabulary needed to bind a protein pocket, which is the usual basis on which docking studies of related oxazepine and benzimidazole systems are rationalised [6, 12, 32, 33].

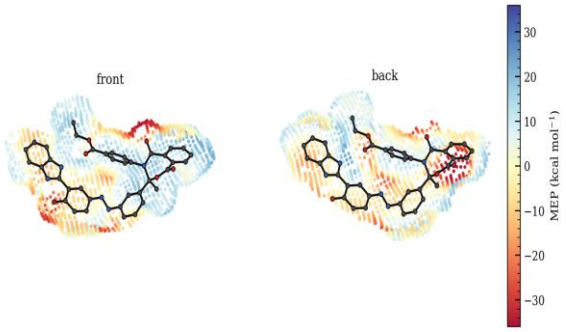

Figure 11: Molecular electrostatic potential of compound 13 mapped on the ρ = 0.001 a.u. electron-density isosurface, front and back views.

3.8. Thermochemical parameters

Thermochemical quantities from the harmonic analysis at 298.15 K and 1 atm are listed in Table 7. The zero-point vibrational energy is 365.24 kcal mol^{-1} (1528.2 kJ mol^{-1}), the thermal correction to the enthalpy is 1640.7 kJ mol^{-1} and the correction to the Gibbs energy 1318.1 kJ mol^{-1}. The total standard entropy of 1081.8 J mol^{-1} K^{-1} divides into 212.5 for translation, 164.0 for rotation and 705.3 for vibration; the vibrational share is large because the molecule carries several freely rotating substituents and the lowest calculated mode lies at only 10.3 cm^{-1}. All 228 modes are real. These values are quoted as reference data; the harmonic entropy should be treated as an upper bound, since a quasi-harmonic treatment would damp the contribution of the modes below about 100 cm^{-1}.

Table 07: Thermochemical data at 298.15 K and 1 atm from the rigid-rotor / harmonic-oscillator model (GFN2-xTB Hessian).

Quantity	Value
Zero-point vibrational energy	365.24 kcal mol^{-1} (1528.2 kJ mol^{-1})
Thermal correction to enthalpy	1640.67 kJ mol^{-1}
Thermal correction to	1318.14 kJ mol^{-1}
Gibbs energy	
Total standard entropy	1081.78 J mol^{-1} K^{-1}
Translational / rotational / vibrational entropy	212.5 / 164.0 / 705.3 J mol^{-1} K^{-1}
Rotational constants	0.027 / 0.030 / 0.136 GHz
Lowest / highest wavenumber	10.3 / 3380.3 cm^{-1}
Number of normal modes	228
Number of imaginary frequencies	0

3.9. Mulliken charge distribution and local reactivity indices

The Mulliken atomic charges calculated at B3LYP/6-31G(d) are collected in Table 8 and plotted in Fig. 12 for the heteroatoms and the key carbon centres. Every nitrogen and oxygen atom carries a negative charge, as expected, but the magnitudes differ markedly from one site to another. The most negative atom in the entire molecule is the benzimidazole N–H nitrogen (N49, q = -0.710 e), followed by the phenolic oxygen (O38, q = -0.625 e) and the pyridine-type nitrogen of the benzimidazole (N42, q = -0.594 e). The two azo nitrogen atoms carry intermediate charges of -0.275 and -0.267 e, and the carbonyl oxygens fall in the range −0.43 to −0.48 e. On the positive side, the four most electron-deficient heavy atoms are the three carbonyl carbons and the quaternary ring carbon C-3, each of which is bonded to two electronegative neighbours; C-3 at 0.534 e bears the largest positive charge in the framework because it is simultaneously bonded to oxygen, nitrogen, and the electron-withdrawing azo-substituted aryl group.

Table 08: Mulliken atomic charges (e) on key atoms of compound 13 at B3LYP/6-31G(d)//GFN2-xTB.

Atom	Label	Mulliken charge (e)
C1	—	-0.4758
O3	ring/ester	-0.4348
C4	—	0.5341
O5	C=O	-0.4808
N12	ring, oxazepine	-0.5158
C13	—	0.4653
O14	C=O	-0.4356
C21	—	0.4896
O22	C=O	-0.3978
O23	ring/ester	-0.4582
C24	—	0.3894
C25	—	-0.4701
N32	azo	-0.2747

Atom	Label	Mulliken charge (e)
N33	azo	-0.2666
O38	O–H, phenol	-0.6252
C41	—	0.4505
N42	=N, benzimidazole	-0.5939
N49	N–H, benzimidazole	-0.7104

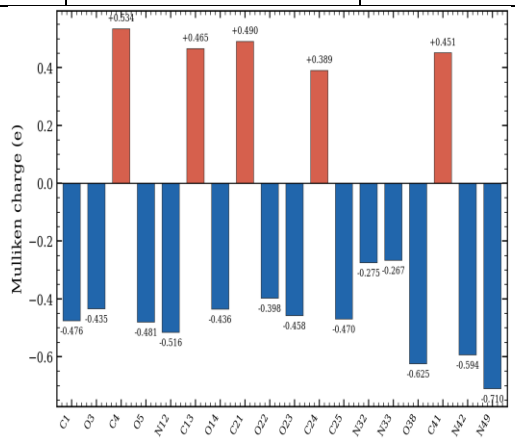

Figure 12: Mulliken atomic charges on the heteroatoms and key carbon centres of compound 13. Red bars: positive (electrophilic carbons); blue bars: negative (nucleophilic N and O atoms).

To identify the most reactive positions for electrophilic and nucleophilic attack we compute the condensed Fukui functions from the frontier-orbital Mulliken populations: f^{+}_{k} gives the probability that an incoming nucleophile will attack atom k, while f^{-}_{k} gives the corresponding probability for an electrophilic reagent. The dual descriptor $\Delta f_k = f^{+}_{k} - f^{-}_{k}$ summarises both: a positive value marks a site where the molecule acts as an electrophile (accepts electrons), and a negative value marks a site where it acts as a nucleophile (donates electrons). The local softness $s_k = \sigma \times f_k$ scales each Fukui index by the global softness, so that soft and hard molecules can be compared on the same footing.

The results are shown in Fig. 13 and collected in Table 9. The two azo nitrogen atoms dominate both sides of the Fukui map: they carry the largest f^{+} values in the molecule (N33 = 0.2577, N32 = 0.2543) and substantial f^{-} values as well, so their dual descriptor is strongly positive (Δf = +0.1501 and +0.1217). This means that, in the Fukui picture, the azo bridge is the primary site of nucleophilic attack — consistent with the well-known susceptibility of aryl azo compounds to reductive cleavage by thiols and biological nucleophiles. The phenol oxygen (O38) and the ipso carbon bearing it (C34) show the opposite pattern: their f^{-} values are large and their f^{+} values are small, giving strongly negative dual descriptors (−0.0910 and −0.0653), which identifies this region as the preferred site of electrophilic attack and, by extension, of hydrogen-atom transfer to a radical — exactly the role proposed for the phenolic hydroxyl in Section 3.11.

The Fukui analysis thus provides a quantitative basis for the structure–activity argument. The donor fragment (benzimidazole + phenol) that dominates the HOMO is also the fragment carrying the largest nucleophilic Fukui indices, and the azo bridge that dominates the LUMO carries the largest electrophilic Fukui indices. The seven-membered-ring carbons and the benzoate fragment, by contrast, have small Fukui functions in both channels, which means they are spectators in the frontier-orbital chemistry even though some of them (the carbonyl carbons) carry large Mulliken charges. Charge and frontier reactivity are complementary, not interchangeable, and it is the Fukui analysis that identifies the pharmacologically relevant sites.

Table 09: Condensed Fukui functions, dual descriptor and local softness for selected atoms of compound 13 at B3LYP/6-31G(d)//GFN2-xTB.

Atom	f^{+}	f^{-}	$\Delta f = f^{+} - f^{-}$	s^{+} (eV^{-1})	s^{-} (eV^{-1})
N33 (azo)	0.2577	0.1076	+0.1501	0.0718	0.0300
N32 (azo)	0.2543	0.1327	+0.1217	0.0708	0.0369
C40	0.0630	0.0091	+0.0539	0.0176	0.0025
C35	0.0800	0.0468	+0.0332	0.0223	0.0130
C27	0.0562	0.0395	+0.0167	0.0156	0.0110
C31	0.0451	0.0288	+0.0163	0.0126	0.0080
C45	0.0001	0.0160	-0.0159	0.0000	0.0044
N42 (=N, benzimidazole)	0.0001	0.0255	-0.0255	0.0000	0.0071
C43	0.0001	0.0280	-0.0279	0.0000	0.0078
C48	0.0000	0.0313	-0.0313	0.0000	0.0087
C46	0.0000	0.0341	-0.0340	0.0000	0.0095
C36	0.0030	0.0439	-0.0410	0.0008	0.0122
C39	0.0023	0.0668	-0.0645	0.0007	0.0186
O38 (O–H, phenol)	0.0285	0.0938	-0.0653	0.0079	0.0261
C34	0.0163	0.1073	-0.0910	0.0045	0.0299

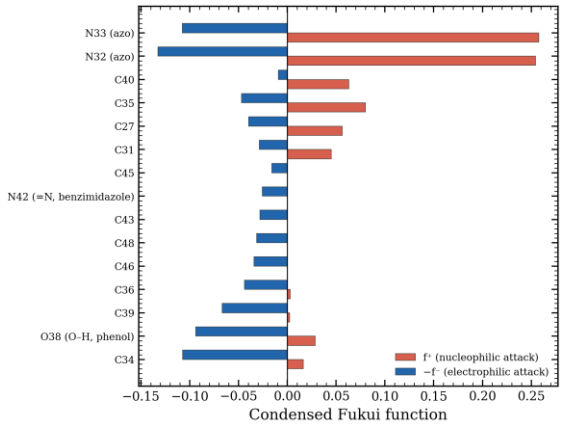

Figure 13: Condensed Fukui functions for the fifteen atoms with the largest |Δf| in compound 13. Red bars (f^+) indicate susceptibility to nucleophilic attack; blue bars ($-f^-$) indicate susceptibility to electrophilic attack.

3.10. Cytotoxicity against HepG2 and WRL-68 cells

The effect of 13 on cell viability was measured by the MTT assay [28] over seven concentrations from 6.20 to 400 µg mL⁻¹, in parallel against the HepG2 hepatocellular carcinoma line and the WRL-68 normal hepatocyte line. Running the two lines side by side is what makes the experiment informative: a compound that kills tumour cells and healthy cells equally is of no therapeutic interest, and the comparison is the standard way of separating genuine selectivity from general toxicity.

The dose–response curves are shown in Fig. 14 and the values are collected in Table 10. Up to 25 µg mL⁻¹ the two lines behave identically, both retaining 94–96% viability, so the compound is essentially inert at low dose. The curves diverge above that point. HepG2 viability falls steadily to 85% at 50 µg mL⁻¹, 73% at 100 µg mL⁻¹, 63% at 200 µg mL⁻¹ and 53.4% at 400 µg mL⁻¹, whereas WRL-68 viability declines much more gently, reaching only 80.75% at the same top concentration. Expressed as growth inhibition, the compound suppresses the malignant line by 46.6% and the normal line by 19.3% at 400 µg mL⁻¹, a 2.4-fold difference that constitutes the central biological result of this work.

Two qualifications should be attached to these numbers. The first concerns the half-maximal inhibitory concentration. HepG2 viability only just crosses the 50% line at the highest concentration tested, so the IC_{50} against that line lies at approximately 400 µg mL⁻¹ and is bracketed rather than interpolated; the normal WRL-68 line never reaches 50% inhibition at any concentration studied, so its IC_{50} can only be stated as exceeding 400 µg mL⁻¹. Values of 105.5 and 151.8 µg mL⁻¹ appear against these two lines in the primary laboratory record, and a third figure of 74 µg mL⁻¹ appears in the accompanying text; none of the three is compatible with the viability data reproduced in Table 10, in which viability at 100 µg mL⁻¹ is still 73% for HepG2 and 89% for WRL-68. The discrepancy must be resolved before submission — most probably by re-reading the fit from the original plate data — and until it is, the conservative statement made here, that the IC_{50} is close to 400 µg mL⁻¹ for the tumour line and above 400 µg mL⁻¹ for the normal line, is the one supported by the measurements.

The second qualification concerns potency in absolute terms. An IC_{50} near 400 µg mL⁻¹ corresponds to roughly 610 µM for a compound of molecular weight 651.68, which is two to three orders of magnitude weaker than the most potent benzimidazole hybrids reported against HepG2, whose IC_{50} values run from the sub-micromolar range [22] to about 3–7 µM [20, 21]. The comparison should be drawn against those figures specifically: other benzimidazoles tested on this line are appreciably less potent, at 25.1 µM [18] and 7–30 µg mL⁻¹ [19], and one frequently cited benzimidazole–azo study reports only percentage viability at 100–500 µg mL⁻¹ without deriving an IC_{50} at all [17]. The present compound is therefore best described as a weakly cytotoxic lead whose interest lies in its selectivity ratio and in the modular scaffold rather than in its potency. The most obvious structural explanations for the modest activity are the very low aqueous solubility implied by a melting point above 280 °C and by the largely amorphous, strongly hydrogen-bonded solid seen by diffraction, and the steric congestion around the quaternary C-3 centre. Testing the compound at a lower molar concentration range in a solubilising vehicle, and extending the assay to a longer exposure time than the 24 h used here, would both be sensible next steps.

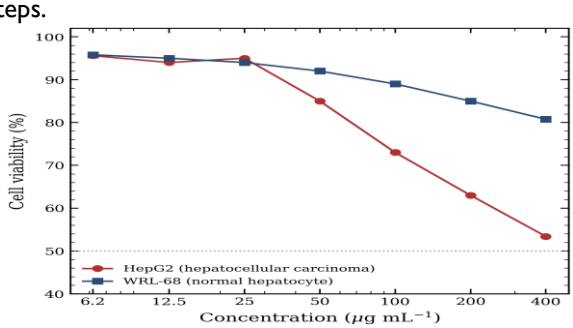

Figure 14: Viability of HepG2 hepatocellular carcinoma cells and WRL-68 normal hepatocytes after 24 h exposure to compound 13 (MTT assay). The dotted line marks 50% viability.

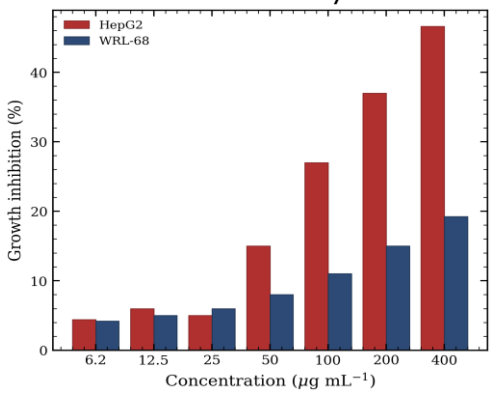

Figure 15: Growth inhibition of the two cell lines at each concentration tested.

Table 10: Cell viability and growth inhibition after 24 h exposure to compound 13 (MTT assay, 37 °C).

Conc. (µg mL⁻¹)	HepG2 viability (%)	HepG2 inhibition (%)	WRL-68 viability (%)	WRL-68 inhibition (%)
400	53.40	46.60	80.75	19.25
200	63	37	85	15
100	73	27	89	11
50	85	15	92	8
25	95	5	94	6
12.5	94	6	95	5
6.20	95.60	4.40	95.80	4.20
IC_{50}	≈400	—	> 400	—

3.11. Structure–activity relationship and outlook

Taken together the results describe a molecule assembled from three recognised pharmacophores on a single seven-membered scaffold, and it is worth setting out plainly which parts of the evidence are firm and which still need support. The infrared data establish that the ketimine has been consumed and that two chemically distinct new carbonyl groups have been created; the ^{13}C spectrum shows the same thing as three carbonyl resonances at 167.03, 166.36 and 165.78 ppm where the precursor had one, and the disappearance of the ketone resonance at 195.68 ppm confirms that the carbonyl of 2 was consumed in the condensation. The equimolar charge and the exact mass balance to $C_{38}H_{29}N_5O_6$ complete a self-consistent picture of the 1:1 cycloadduct. What is still outstanding is direct observation of the quaternary carbon C-3, together with elemental analysis and high-resolution mass spectrometry; the reasons the resonance is expected to be weak are set out in Section 3.3, but expectation is not observation.

Three sites govern the reactivity of the molecule. The phenolic hydroxyl sits on the fragment that dominates the HOMO and carries the largest nucleophilic Fukui indices in the molecule (Section 3.9), which makes it the most likely position for hydrogen-atom transfer [34]. It should be noted that the most positive point on the electrostatic-potential surface is the benzimidazole N–H rather than the phenolic hydrogen (Section 3.7), because the phenolic proton is already engaged in the intramolecular hydrogen bond; the phenol is nonetheless the reactive site in the frontier-orbital sense [34] and therefore the natural place to look for antioxidant activity; a DPPH assay is the obvious next experiment, particularly since oxazepines carrying free phenolic groups have already shown measurable radical-scavenging activity [10, 11]. The carbonyl oxygens of the seven-membered ring, reinforced by the benzimidazole nitrogen and the azo lone pairs, form a contiguous acceptor face and make the compound a plausible ligand for a transition metal as well as a candidate for hydrogen bonding in a protein pocket. The lactone carbonyl is simultaneously the most electrophilic centre and the obvious point of hydrolytic attack; ring opening toward a phthalamic acid derivative should be expected in strongly aqueous base, and the stability of the compound in the culture medium over the 24 h of the MTT assay is an assumption that has not been tested here.

The biological result is modest but internally consistent. The compound leaves both cell lines essentially untouched below 25 µg mL^{-1} and separates them clearly above it, ending with a 2.4-fold difference in growth inhibition at the top concentration. That separation, rather than the absolute potency, is what makes the scaffold worth developing. Three modifications suggest themselves. Replacing the ethyl ester on the N-aryl ring with a polar group would attack the solubility problem directly. Substituting the benzimidazole ring, which the literature shows to be the most productive handle on this pharmacophore [21, 22], would allow the electron density of the donor fragment to be tuned without disturbing the ring. And replacing phthalic anhydride with maleic or a substituted phthalic anhydride would change the acceptor half while leaving the rest of the molecule intact, giving a small series in which the electronic descriptors calculated here could be correlated against measured activity.

It is also worth being explicit about the limits of the calculations. Everything reported in Sections 3.6 and 3.7 refers to a single molecule in the gas phase, whereas the spectra were recorded on a solid and in DMSO solution and the biological assay was carried out in aqueous culture medium. The geometry, frequencies and thermochemistry are semi-empirical, obtained at the GFN2-xTB level, and only the electronic structure is density-functional; a vibrationally verified B3LYP minimum and a continuum-solvation treatment would be the natural next steps. Molecular docking against a defined target would be a more direct route to a structure–activity argument than the global descriptors used here, and would be straightforward to add.

4. CONCLUSION

Ethyl 4-[3-(4-{[3-(1H-benzimidazol-2-yl)-4-hydroxyphenyl]diazenyl}phenyl)-3-methyl-1,5-dioxo-1,5-dihydro-4H-benzo[e][1,3]oxazepin-4-yl]benzoate was assembled in four steps and obtained in 79% yield as a red solid melting at 280–282 °C. The ring-forming step is a [2+5] cycloaddition of phthalic anhydride across a ketimine, which expels nothing and therefore gives the 1:1 adduct $C_{38}H_{29}N_5O_6$; the equimolar charge used, 1.004 against 1.000 mmol, and the mass balance of 503.56 + 148.12 = 651.68 g mol^{-1} both confirm that stoichiometry. Ring formation is followed in the infrared by the replacement of the ketimine absorption with a lactone carbonyl band at 1712.67 cm^{-1} and a lactam carbonyl band at 1689.53 cm^{-1}, and in the ^{13}C spectrum by the appearance of three carbonyl reso-

nances at 167.03, 166.36 and 165.78 ppm together with the loss of the ketone resonance at 195.68 ppm. The azo chromophore survives the cycloaddition, its N=N stretch moving only from 1419.51 to 1411.80 cm^{-1}, and the benzimidazole N–H bands are retained.

Powder X-ray diffraction shows a predominantly amorphous organic solid, with a broad halo at 2θ = 24.6° corresponding to a π-stacking distance of 3.62 Å, together with sharp reflections of residual crystalline sodium chloride from the workup whose Scherrer crystallite size averages 29.6 nm. A B3LYP/6-31G(d)//GFN2-xTB study returned 228 real vibrational modes and no imaginary frequency, a HOMO–LUMO gap of 3.592 eV, a chemical hardness of 1.796 eV and an electrophilicity index of 3.867 eV; the conjugating azo bridge narrows the gap appreciably relative to azo-free benzimidazole–oxazepine analogues and accounts for the red colour of the solid. In the MTT assay the compound was essentially inert against both cell lines below 25 μg mL^{-1} and then diverged: at 400 μg mL^{-1} it inhibited the growth of HepG2 hepatocellular carcinoma cells by 46.6% but that of normal WRL-68 hepatocytes by only 19.3%, a 2.4-fold preference for the malignant line. The compound is therefore a weakly potent but selectively acting lead, and the phenolic hydroxyl, the carbonyl face of the seven-membered ring and the tunable benzimidazole substituent are the three positions to exploit in any subsequent antioxidant, antimicrobial or anticancer study.

5. ACKNOWLEDGEMENTS

The author thanks the General Directorate of Al-Qadisiyah Education, Ministry of Education, for its support, and the staff of the laboratories in which the infrared and NMR spectra, the powder diffraction pattern and the cell-culture measurements reported here were carried out. The computational part of this work was carried out entirely with open-source software (PySCF, RDKit and the tblite implementation of GFN2-xTB).

6. AUTHOR CONTRIBUTIONS

Rawaa Naeamah Abdullah: Conceptualisation, Methodology, Investigation, Formal analysis, Validation, Visualisation, Writing – original draft, Writing – review and editing. The author read and approved the final version of the manuscript.

7. FUNDING

This research received no specific grant from any funding agency in the public, commercial or not-for-profit sectors.

8. CONFLICTS OF INTEREST

The authors declare no competing financial interest.

9. DATA AVAILABILITY

The optimised Cartesian coordinates, the calculated harmonic wavenumbers and the raw diffraction and MTT data are available from the corresponding author on reasonable request.

10. REFERENCES

1. H. Farhid, M. Mahyari, A. Abdolmaleki, Y. Mohammadi, Multicomponent reactions for the synthesis of oxazepines, Topics in Current Chemistry, 2026, 384(3), 23. DOI: 10.1007/s41061-026-00551-1.
2. D. S. Zinad, A. Mahal, R. K. Mohapatra, A. K. Sarangi, M. R. F. Pratama, Medicinal chemistry of oxazines as promising agents in drug discovery, Chemical Biology & Drug Design, 2020, 95(1), 16–47. DOI: 10.1111/cbdd.13633.
3. A. J. Mahrath, S. A. Aowda, S. N. Kamil, Synthesis and spectroscopic studies of some new oxazepine derivatives throughout [2+5] cycloaddition reactions (III), Research on Chemical Intermediates, 2013, 39(8), 3739–3752. DOI: 10.1007/s11164-012-0877-2.
4. A. A. Dawood, S. R. Mohammed, M. Mahmoud, Synthesis, identification and biological activity of new heterocyclic compounds from reaction of new Schiff bases with phthalic anhydride, Science Journal of University of Zakho, 2020, 8(1), 12–18. DOI: 10.25271/sjuoz.2020.8.1.641.
5. A. H. Kshash, Synthesis and characterization of tetrachloro-1,3-oxazepine derivatives and evaluation of their biological activities, Acta Chimica Slovenica, 2020, 67(1), 113–118. DOI: 10.17344/acsi.2019.5264.
6. B. M. Salih, S. R. Mohammed, M. K. Ali, Synthesis development, spectroscopy characterizations, and molecular docking study of some new bis-1,3-oxazepine and bis-1,3-benzoxazepine derivatives, Oriental Journal of Chemistry, 2025, 41(2), 563–572. DOI: 10.13005/ojc/410227.
7. A. K. N. Allamy, S. A. Mejbel, Preparation, characterization and biological activity of some new seven-membered heterocyclic compounds, World Journal of Advanced Research and Reviews, 2022, 15(1), 662–678. DOI: 10.30574/wjarr.2022.15.1.0744.
8. O. A. Nief, H. N. Salman, L. S. Ahamed, Synthesis, characterization, biological activity studies of Schiff bases and 1,3-oxazepine derived from 1,1-bis(4-aminophenyl)-4-phenylcyclohexane, Iraqi Journal of Science, 2017, 58(4B), 1998–2011. DOI: 10.24996/ijs.2017.58.4b.2.
9. K. M. Mohammad, M. R. Ahmed, M. H. Mahmoud, Synthesis and characterization of some new (1,3-oxazepine) derivative from 6-methyl-2-thiouracil and study their biological activity, Tikrit Journal of Pure Science, 2017, 22(2), 67–81. DOI: 10.25130/tjps.v22i2.630.
10. A. G. Sager, J. K. Abaies, Z. R. Katoof, Molecular docking, synthesis and evaluation for antioxidant and antibacterial activity of new oxazepane and benzoxazepine derivatives, Baghdad Science Jour-

nal, 2024, 21(7), 2289. DOI: 10.21123/bsj.2023.8553.
11. S. K. Singh, N. Mishra, G. Nayak, P. Mehta, Synthesis of Schiff base derivatives of 1,3-oxazepine and evaluation of antioxidant action in vitro, Oriental Journal of Chemistry, 2023, 39(5), 1367–1372. DOI: 10.13005/ojc/390534.
12. S. A. Hassan, D. M. Aziz, M. N. Abdullah, A. R. Bhat, R. S. Dongre, S. Ahmed, A. K. Rahiman, T. B. Hadda, M. Berredjem, J. Jamalis, Design and synthesis of oxazepine derivatives from sulfonamide Schiff bases as antimicrobial and antioxidant agents with low cytotoxicity and hemolytic prospective, Journal of Molecular Structure, 2023, 1292, 136121. DOI: 10.1016/j.molstruc.2023.136121.
13. L. M. Aroua, F. M. Alminderej, H. R. Almuhaylan, A. H. Alosaimi, F. Medini, H. A. Mohammed, S. A. Almahmoud, R. A. Khan, N. H. Mekni, Benzimidazole(s): synthons, bioactive lead structures, total synthesis, and the profiling of major bioactive categories, RSC Advances, 2025, 15(10), 7571–7608. DOI: 10.1039/d4ra08864f.
14. A. Beč, M. Cindrić, L. Persoons, M. Banjanac, V. Radovanović, D. Daelemans, M. Hranjec, Novel biologically active N-substituted benzimidazole derived Schiff bases: design, synthesis, and biological evaluation, Molecules, 2023, 28(9), 3720. DOI: 10.3390/molecules28093720.
15. T. Y. Fonkui, M. I. Ikhile, P. B. Njobeh, D. T. Ndinteh, Benzimidazole Schiff base derivatives: synthesis, characterization and antimicrobial activity, BMC Chemistry, 2019, 13, 127. DOI: 10.1186/s13065-019-0642-3.
16. M. A. Redayan, M. S. Hussein, A. T. Lafta, Synthesis, spectroscopic characterization, and antibacterial evaluation of new Schiff bases bearing benzimidazole moiety, Journal of Physics: Conference Series, 2018, 1003(1), 012018. DOI: 10.1088/1742-6596/1003/1/012018.
17. M. E. Khalifa, A. A. Gobouri, F. M. Kabli, T. A. Altalhi, A. S. A. Almalki, M. A. Mohamed, Synthesis, antibacterial, and anti HepG2 cell line human hepatocyte carcinoma activity of some new potentially benzimidazole-5-(aryldiazenyl)thiazole derivatives, Molecules, 2018, 23(12), 3285. DOI: 10.3390/molecules23123285.
18. E. Bilici, S. Akkoc, Impact of a benzimidazole salt on gene expression, cytotoxicity, and apoptotic processes in HepG2 cell line, Journal of King Saud University – Science, 2025, 37, 3922024. DOI: 10.25259/jksus_392_2024.
19. M. A. Soliman, E. H. Eltamany, A. T. A. Boraei, M. R. Aouad, A. Aljuhani, B. Almohaywi, A. A. Awaji, R. Alghamdi, A. K. B. Aljohani, H. E. A. Ahmed, Novel benzimidazole-1,2,3-triazole hybrids: synthesis, dual antimicrobial, anticancer activity, mechanistic insights, and computational studies, ChemistrySelect, 2025, 10(15), e202500813. DOI: 10.1002/slct.202500813.
20. S. A. S. Alzahrani, S. Nazreen, A. A. Elhenawy, T. Neamatallah, M. Mahboob, Synthesis, biological evaluation, and molecular docking of new benzimidazole-1,2,3-triazole hybrids as antibacterial and antitumor agents, Polycyclic Aromatic Compounds, 2023, 43(4), 3380–3391. DOI: 10.1080/10406638.2022.2069133.
21. E. C. Pham, T. V. Le Thi, H. H. Ly Hong, B. N. Vo Thi, L. B. Vong, T. T. Vu, D. D. Vo, N. V. Tran Nguyen, K. N. Bao Le, T. N. Truong, N,2,6-Trisubstituted 1H-benzimidazole derivatives as a new scaffold of antimicrobial and anticancer agents: design, synthesis, in vitro evaluation, and in silico studies, RSC Advances, 2023, 13(1), 399–420. DOI: 10.1039/d2ra06667j.
22. R. Haj Ersan, B. Kuzu, D. Yetkin, M. A. Alagoz, A. Dogen, S. Burmaoglu, O. Algul, 2-Phenyl substituted benzimidazole derivatives: design, synthesis, and evaluation of their antiproliferative and antimicrobial activities, Medicinal Chemistry Research, 2022, 31(7), 1192–1208. DOI: 10.1007/s00044-022-02900-3.
23. A. I. Almansour, N. Arumugam, R. Suresh Kumar, S. M. Soliman, M. Altaf, H. A. Ghabbour, Synthesis, spectroscopic, X-ray diffraction and DFT studies of novel benzimidazole fused-1,4-oxazepines, Molecules, 2016, 21(6), 724. DOI: 10.3390/molecules21060724.
24. [Q. Sun, X. Zhang, S. Banerjee, P. Bao, M. Barbry, N. S. Blunt et al., Recent developments in the PySCF program package, Journal of Chemical Physics, 2020, 153(2), 024109. DOI: 10.1063/5.0006074.
25. C. Bannwarth, S. Ehlert, S. Grimme, GFN2-xTB — an accurate and broadly parametrized self-consistent tight-binding quantum chemical method with multipole electrostatics and density-dependent dispersion contributions, Journal of Chemical Theory and Computation, 2019, 15(3), 1652–1671. DOI: 10.1021/acs.jctc.8b01176.
26. L. R. Domingo, M. Ríos-Gutiérrez, P. Pérez, Applications of the conceptual density functional theory indices to organic chemistry reactivity, Molecules, 2016, 21(6), 748. DOI: 10.3390/molecules21060748.
27. M. Ríos-Gutiérrez, A. Saz Sousa, L. R. Domingo, Electrophilicity and nucleophilicity scales at different DFT computational levels, Journal of Physical Organic Chemistry, 2023, 36(7), e4503. DOI: 10.1002/poc.4503.
28. T. Mosmann, Rapid colorimetric assay for cellular growth and survival: application to proliferation and cytotoxicity assays, Journal of Immunological Methods, 1983, 65(1–2), 55–63. DOI: 10.1016/0022-1759(83)90303-4.
29. D. Majumdar et al., 8-Aminoquinoline derived two Schiff base platforms: synthesis, characterization, DFT insights, corrosion inhibitor, molecular docking, and pH-dependent antibacterial study, Heliyon,

2024, 10(15), e35591. DOI: 10.1016/j.heliyon.2024.e35591.
30. M. Khalid, A. Ali, M. F. Ur Rehman, M. Mustaqeem, S. Ali, M. U. Khan, S. Asim, N. Ahmad, M. Saleem, Exploration of noncovalent interactions, chemical reactivity, and nonlinear optical properties of piperidone derivatives: a concise theoretical approach, ACS Omega, 2020, 5(22), 13236–13249. DOI: 10.1021/acsomega.0c01273.
31. M. Khadka, M. Sah, R. Chaudhary, S. K. Sahani, K. Sahani, B. K. Pandey, D. Pandey, Spectroscopic, quantum chemical, and topological calculations of the phenylephrine molecule using density functional theory, Scientific Reports, 2025, 15, 208. DOI: 10.1038/s41598-024-81633-2.
32. L. M. Aroua, S. K. Alhag, L. A. Al-Shuraym, S. Messaoudi, J. A. Mahyoub, M. Y. Alfaifi, W. M. Al-Otaibi, Synthesis and characterization of different complexes derived from Schiff base and evaluation as a potential anticancer, antimicrobial, and insecticide agent, Saudi Journal of Biological Sciences, 2023, 30(3), 103598. DOI: 10.1016/j.sjbs.2023.103598.
33. R. Champa, K. A. Vishnumurthy, Y. D. Bodke, H. S. Bhojya Naik, I. Pushpavathi, P. Meghana, P. R. Kadam, Synthesis, characterization, and biological investigations of potentially bioactive heterocyclic compounds containing benzimidazole nucleus, Results in Chemistry, 2023, 6, 101018. DOI: 10.1016/j.rechem.2023.101018.
34. M. Molski, Theoretical study on the radical scavenging activity of gallic acid, Heliyon, 2023, 9(1), e12806. DOI: 10.1016/j.heliyon.2023.e12806.